High-Spatial-Resolution Coherent Doppler Lidar With Pseudo-Random Phase-Shift Keying

Yunpeng Zhang, Yunbin Wu, and Haiyun Xia

***Abstract*— A high-spatial-resolution coherent Doppler wind lidar (CDWL) incorporating pseudo-random phase-shift keying (PR-PSK) modulation is proposed and demonstrated. The pseudo-random phase coding technique can enhance the spatial resolution without broadening the backscattered spectrum but suffers from the non-instantaneous transition edges caused by the limited bandwidth. In this work, ideal binary PSK modulation is achieved by exploiting the zero crossing of the Mach-Zehnder modulator's (MZM) transfer function, thus greatly reducing the bandwidth requirement. The amplitude shaping and phase modulation of the pulses are naturally aligned as they are realized together in one MZM. Meanwhile, a real-time bias monitoring scheme for the MZM is proposed to facilitate engineering applications. At laser peak power of 300 W, continuous radial wind profile measurement in 800 m is demonstrated, with spatial/temporal resolution of 3 m/0.5 s.**

***Index Terms*— Doppler wind lidar, spatial resolution, phase shift keying, pseudo-random code.**

I. Introduction

As a powerful remote sensing technique, Doppler wind lidar has been widely applied in scientific researches and engineering applications, such as gravity waves monitoring [1], wind energy exploitation [2], and air pollution analysis [3]. When assisted by the coherent detection, a coherent Doppler wind lidar (CDWL) provides the range resolved atmospheric backscattered spectra, which can be used for spectrum-based applications like raindrop size distribution analysis [4]. To further promote the CDWL in areas like aviation safety and turbulence detection [5], [6], higher spatial resolution is demanded. The resolution of 3 m could be realized with a conventional pulsed CDWL at the sacrifice of detection range [7]. When raising the spatial resolution of a conventional pulsed lidar, the spectrum broadening and low carrier-to-noise ratio (CNR) would reduce the detection accuracy [8].

Manuscript received 19 June 2022; revised 13 February 2023; accepted 30 March 2023. Date of publication 3 April 2023; date of current version 7 April 2023. This work was supported by the National Ten Thousand Talent Program in China and Strategic Priority Research Program of Chinese Academy of Sciences under Grant XDA22040601. *(Corresponding author: Haiyun Xia.)*

Yunpeng Zhang and Yunbin Wu are with the School of Earth and Space Sciences, University of Science and Technology of China (USTC), Hefei 230026, China (e-mail: zyp110@mail.ustc.edu.cn; wuyunbin@mail.ustc.edu.cn).

Haiyun Xia is with the School of Earth and Space Sciences and the Hefei National Laboratory for Physical Sciences at the Microscale, University of Science and Technology of China (USTC), Hefei 230026, China, also with the School of Atmospheric Physics, Nanjing University of Information Science and Technology, Nanjing 210044, China, and also with the Institute of Software, Chinese Academy of Sciences, Beijing 100190, China (e-mail: hsia@ustc.edu.cn).

Color versions of one or more figures in this letter are available at https://doi.org/10.1109/LPT.2023.3264239.

Digital Object Identifier 10.1109/LPT.2023.3264239

Recently, several methods have been proposed to overcome these obstacles. The differential correlation pair (DCP) method realizes a spatial resolution of 3 m by employing paired pulses [9], [10], while the spatial resolution is determined by the duration of the short probing pulse. As the difference is conducted on the cross-correlation, a too short probing pulse may be seriously interfered by the long common pulse. Meanwhile, the pseudo-random phase coding (PRPC) method decouples the spatial resolution and pulse duration by the spread-spectrum property of the pseudo-random code [11], [12], and realizes the spatial resolution of 4.5 m in wind sensing. However, a very high analog bandwidth is required to support the fast phase switches. Moreover, as the half-wave voltage of the phase modulator changes with the temperature, without a precise temperature control, an imperfect phase modulation would degrade the spatial resolution [13].

To solve these problems, we propose and demonstrate a CDWL with pseudo-random phase-shift keying (PR-PSK) modulation in this work. The ideal binary PSK modulation is achieved with a Mach-Zehnder modulator (MZM) through the zero crossing of the transfer function. Meanwhile, the pulse shaping and PSK modulation are self-aligned, as they are both realized by a single MZM. In addition, a bias monitoring method of the MZM is proposed to facilitate the practical applications.

II. Principle and System

Typically, the transfer function of an electro-optic modulator in Mach-Zehnder configuration can be expressed as [13]:

$$h\left[V_m\left(t\right)\right] = \exp\left(j\phi_0\right)\cos\left[\frac{\pi}{2}\frac{V_m\left(t\right)+V_{DC}}{V_\pi}\right], \tag{1}$$

where $V_m(t)$ is the modulation voltage, V_{DC} is the DC offset, V_π is the half-wave voltage, and ϕ_0 is the common phase shift introduced by the modulator, which can be simply set to π with no losing of generality. When the modulator is biased at the null point ($V_{DC} = V_\pi$), the transfer function can be simplified as:

$$h\left[V_m\left(t\right)\right] = \sin\left[\frac{\pi}{2}\frac{V_m(t)}{V_\pi}\right] = sgn\left[V_m\left(t\right)\right]\cdot\sin\left[\frac{\pi}{2}\left|\frac{V_m\left(t\right)}{V_\pi}\right|\right]. \tag{2}$$

As indicated by (2), the sign of the output lightwave will follow the sign of the modulation voltage. In other words, the ideal binary PSK modulation of 0 or π would be introduced into the lightwave according to the sign of the modulation voltage. Note that conventional phase modulators need the

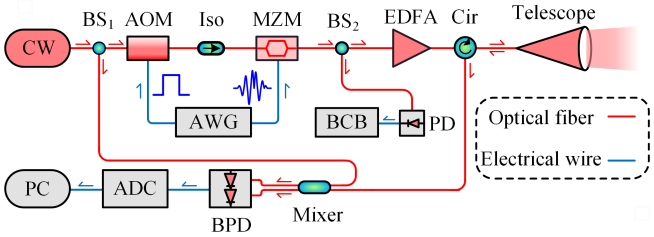

Fig. 1. System layout of the PR-PSK lidar. CW, continuous-wave laser; BS, beam splitter; Iso, isolator; AOM, acousto–optic modulator; MZM, Mach-Zehnder modulator; EDFA, erbium-doped fiber amplifier; Cir, circulator; PD, photodetector; BPD, balanced photodetector; ADC, analog-to-digital converter; AWG, arbitrary waveform generator; BCB, bias control board; and PC, personal computer.

driving signal to change by a half-wave voltage to realize a phase shift of π [12]. In an MZM, as the π phase shift is completed simultaneously with moment when the driving signal crosses zero, the bandwidth requirement is greatly reduced [13]. In addition, since the modulation voltage's sign doesn't affect the magnitude of the transfer function, the intensity of the pulses phased with either 0 or π should be the same.

When DC offset drift happens, $V_{DC} = V_\pi + V_b$, where $V_b$is the bias drift. The intensity of the lightwave phased with 0 or π is:

$$I_\pm = I_0 \sin^2 \left\{ \frac{\pi}{2V_\pi} \left[V_b \pm |V_m(t)| \right] \right\}, \tag{3}$$

where $I_0$is the intensity of the lightwave entering the MZM, and the "+" and "-" correspond to the phases of 0 and π, respectively. The intensity envelopes of the lightwave with 0 and π phases are no longer the same when $V_b \neq 0$, which offers a monitoring point of the MZM's bias.

The system layout of the PR-PSK lidar is shown in Fig. 1. In the transmitter, a 1550-nm continuous-wave laser (Amonics ALiDAR-150-Seed) is split into two parts, with the major and minor portions serving as the master oscillator (MO) of the transmitted signal and the local oscillator (LO), respectively. The MO is chopped into pulses with repetition rate of 25 kHz by an acousto-optic modulator (AOM). Meanwhile, a frequency shift of 80 MHz is introduced. The pulse shaping and PSK modulation are realized by an electro-optic MZM (iXblue MXER-LN-10). The driving signals of the MZM are prestored in an arbitrary waveform generator (AWG, Keysight 33622A) and synchronized with the AOM. A small portion of the modulated signal is detected by a photodetector (PD, Alphalas UPD-15-IR2) to monitor the bias drift of the MZM. A high-power erbium-doped fiber amplifier (EDFA, Amonics ALiDAR-150-AMP) is employed to enhance the pulses' peak power to 300 W. After amplification, the modulated pulses are transmitted to the atmosphere by a 100-mm telescope, which is also used to collect the atmospheric backscattered signal. In the receiver, guided by a circulator, the received optical signal is mixed with the LO and down converted into electrical signal in intermediate frequency (IF) band after beating on a balanced photodetector (BPD). The high isolation of the circulator is crucial in the suppression of amplified spontaneous emission (ASE) noise [14]. The analog bandwidth of the receiver is limited to 220 MHz to avoid frequency

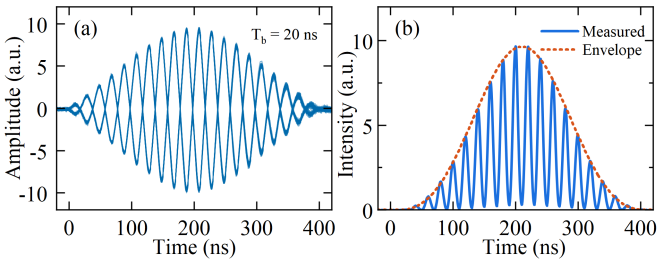

Fig. 2. (a) Eye diagram of the modulated pulses' electric field with $T_b = 20$ ns and $N_s = 20$; (b) Pulse intensity waveform and its envelope.

aliasing when digitized by an analog-to-digital converter (ADC) at 500 MSps. The raw data are stored in a computer for offline processing.

The driving signal of the MZM is a key issue in the system. Each pulse is composed of N_s sub-pulses with the truncated length of T_b. The pulse envelope is set to be a Gaussian function, where the sinusoidal transfer function in (2) should be taken into consideration to get the magnitude of the driving signal. Meanwhile, the sign of the driving signal is generated from a 12-bit m-sequence, where the "0" and "1" are mapped to positive and negative of the modulation voltage. To get the range resolved spectra, the backscattered signal would be gated and decoded with the same m-sequence as used in the modulation. More specific description of the algorithm has been introduced in [12]. As the method inherits the pseudo-random phase modulation principle, the spatial resolution Δz is determined by the T_b according to$\Delta z = cT_b/2$, where c is the speed of light in the atmosphere [12].

Fig. 2(a) shows the eye diagram of the modulated lightwave measured in an experiment with $T_b = 20$ ns and $N_s = 20$. To form the eye diagram, electric field waveforms of 100 pulses are overlapped in the figure. As the amplitude and phase modulation are both conducted by a single MZM, they are naturally aligned. Considering the possible optical pulse jitter [15], the self-alignment can avoid the error caused by the misalignment of the pulse intensity envelope and modulated phase, especially in a high-spatial-resolution lidar. Since the difference between each modulated pulse only exists in the phase, their share the same intensity waveform as shown in Fig. 2(b). The full width at half maximum (FWHM) of the intensity waveform's envelope is measured to be 170 ns. As the laser's linewidth is only 15 kHz, very little phase noise would be introduced in such a short duration.

To ensure that the MZM is correctly biased at the null point, the intensity difference indicated in (3) is considered. Providing $|V_b| + |V_m(t)| \leq V_\pi$, the mean intensity of the lightwave with 0 phase will larger than that of the lightwave with π phase when $V_b > 0$, and vice versa. The bias control board measures and calculates the ratio of the mean intensity of the lightwave with 0 and π phases, which indicates the magnitude and direction of the bias drift. The intensity waveforms at different bias voltages are measured in the experiment. As shown in Fig. 3(a), the ratio of the mean intensity in dB unit is approximately linear to the bias voltage, with the slope got by a linear regression being 3.27 dB/V. To further test the monitoring scheme, intentional disturbances are applied on the DC offset in a step of 0.1 V. Under the

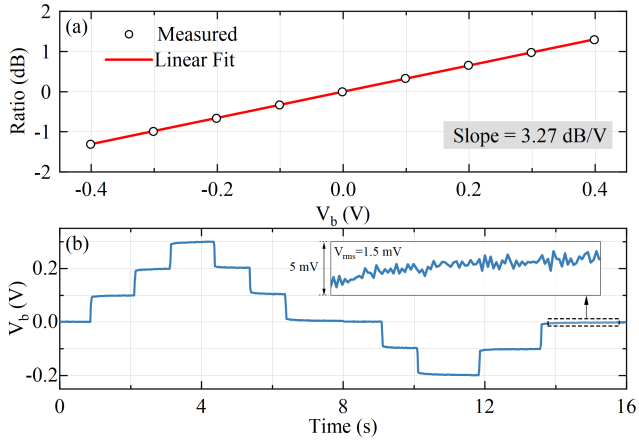

Fig. 3. (a) Ratio of the mean intensity of the lightwave with 0 and π phases at different bias voltages. (b) Real-time monitoring of the bias drift under intentional disturbances.

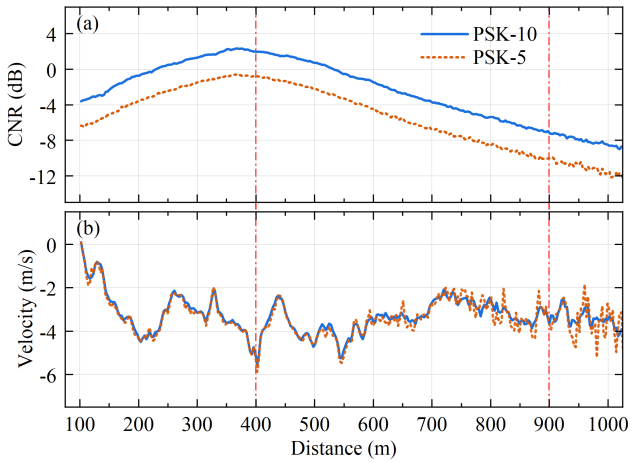

Fig. 4. (a) Narrowband CNR and (b) radial wind velocity profiles of the PR-PSK lidars.

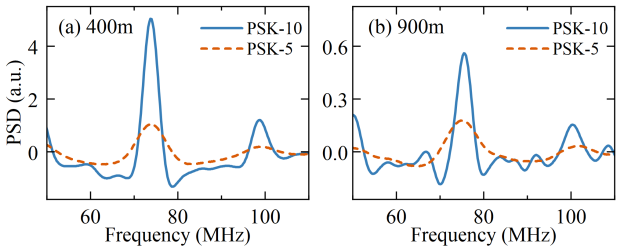

Fig. 5. Spectra of the PR-PSK lidars at (a) 400 m and (b) 900 m.

averaging time of 20 ms, the retrieved bias drift is displayed in Fig. 3(b), where the intentional disturbances are detected with the root mean square (RMS) error of 1.5 mV. And the response time is less than two averaging periods (40 ms). Once a feedback control was added, the bias voltage can be maintained around zero.

III. Experiment and Discussions

During the experiments, the system is placed on the 9th floor of the laboratory building with the telescope pointing to the south at an elevation angle of 15°. In the transmitter, while the modulation bit interval T_b is directly linked to the spatial resolution, the pulse duration, or equivalently, the number of sub-pulses in one pulse is configurable under a specific spatial resolution. In fact, the design of the pulse duration is a comprehensive work. On one hand, a longer pulse leads to higher pulse energy under limited peak power. On the other hand, as the specular reflection from output optics could saturate the receiver [16], a long pulse in the coaxial configuration will increase the blind distance. In addition, the phase noise related to the laser linewidth also needs to be considered when extending the pulse duration. Trade-offs need to be made based on the requirement. In the receiver, after collecting the raw data in time domain, the range resolved spectrum can be got by the periodogram [17]. For each spectrum, the fast Fourier transform (FFT) length is extended to 2048 through zero padding with frequency sampling interval of 0.244 MHz. The temporal resolution is set to be 0.5 s, incoherently averaging the backscattered spectra of 12.5k pulses.

In a first experiment, the performance of the PR-PSK lidar with different intensity envelopes is compared at the same spatial resolution of 6 m, leading to the modulation bit interval (T_b) of 40 ns. And the numbers of sub-pulses in one pulse (N_s) are set to be 10 and 5, respectively. For brevity, the two systems will be called as PSK-10 and PSK-5. The wind profiling results of the two lidars are plotted in Fig. 4, where the blue solid line and orange short-dash line stand for the PSK-10 and PSK-5, respectively.

As shown in Fig. 4(a), the PSK-10 has higher narrowband CNR [8] compared with PSK-5 at the same spatial resolution and laser peak power. One main cause for the difference in CNR is the lower pulse energy of the PSK-5, which is inevitable under a limited laser peak power. Fig. 4(b) shows the radial wind profiles measured by the two lidars, where the wind velocity is derived from the Doppler frequency shift estimated by the Gaussian fit. The two profiles are consistent with each other within 600 m. On the contrast, beyond 600 m, the profile of PSK-5 fluctuates around that of PSK-10.

The signal spectra of the two measurements are shown in Fig. 5, where the spectrum difference technique [12] is used. Harmonic components can be observed at ±25 MHz away from the main peak. Due to the longer pulse duration, the main spectral peak of the PSK-10 is narrower compared to the PSK-5. Meanwhile, the shorter pulse duration of the PSK-5 also reduces the power of the backscattered signal, as illustrated in Fig. 5. The relatively wide spectrum and low CNR explicate the fluctuations in Fig. 4(b).

In a second experiment, the PR-PSK lidar is operated under a high spatial resolution of 3 m, with $T_b = 20$ ns and $N_s = 20$. The transmitted waveform has been shown in Fig. 2. As a reference, a CDWL based on the conventional non-coding (NC) method is employed to validate the measurement of the PR-PSK lidar. The pulse's intensity envelope in the NC lidar is set to be the same as the PR-PSK lidar with the FWHM of 170 ns.

The wind velocity profiles obtained by the two methods are shown in Fig. 6, where the blue marked line and black dashed line denote the measurements by the PR-PSK and NC lidar, respectively. In the continuous profiling for 2 s, the two sets of lines have the same trend versus distance. Differences between the two lidars' measurements exist at some distances, which can be interpreted as the result of the spatial smoothing

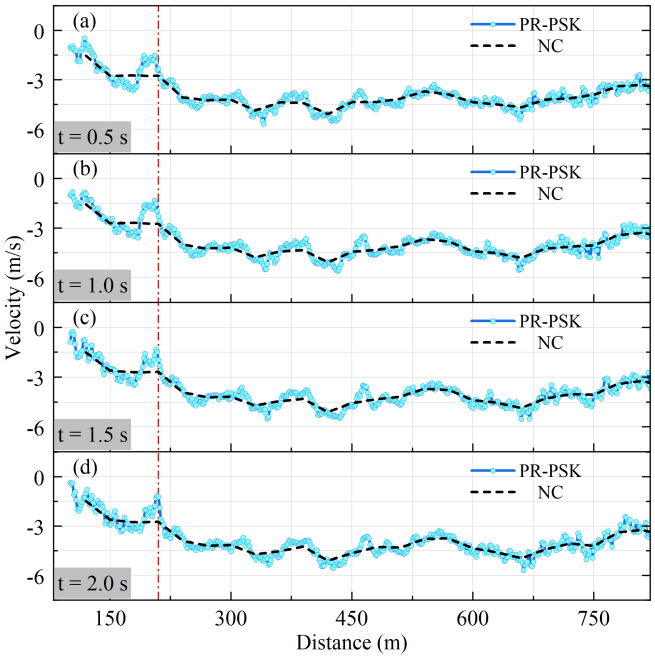

Fig. 6. Radial wind velocity profiles obtained by continuous observation for 2 s.

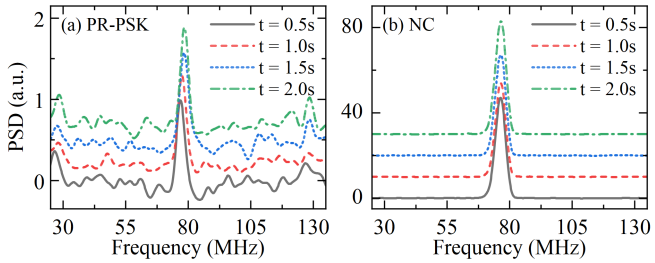

Fig. 7. Spectra continuously measured by the (a) PR-PSK and (b) NC lidars.

effect [10]. The actual wind profile would be smoothed in the scale of spatial resolution. At lower spatial resolution, the fine structure of the wind field details would be wiped out by the NC lidar.

Fig. 7 shows the backscattered spectra at 210 m (marked by the red dash-dot line in Fig. 6) away from the telescope, where the difference between the two measurements occurs. The curves corresponding to the spectra at different time are shifted in the y-axis for clarity. The spectra of the PR-PSK lidar change continuously through time. This continuity further suggests that the difference is more likely to be the time-varying characteristics of the fine wind field rather than the random measurement noise. As the pulse widths in the two lidars are similar, the spectral widths are close as one may expect, though their spatial resolutions are quite different. Thus, the PR-PSK lidar realizes a relatively high spatial resolution while avoiding the spectrum broadening effect.

IV. Conclusion

A CDWL with meter-scale spatial resolution incorporating pseudo-random phase-shift keying is demonstrated. The amplitude shaping and self-aligned phase modulation are realized by an MZM biased at the null point. Since the phase of the modulated lightwave is directly related to the sign rather than the magnitude of the MZM's driving voltage, the rectangular phase switches can be achieved at a relatively low bandwidth requirement compared with the original PRPC method in [12]. Additionally, the proposed MZM bias monitoring scheme could improve the system stability under a practical situation.

In experiments, the performance of the proposed system was tested under different intensity envelopes. Continuous radial wind sensing in 800 m is realized at resolution of 3 m/0.5 s, with the pulse energy, laser peak and average power being 24 μJ, 300 W, and 0.6 W, respectively. Considering the robustness against disturbance, the system has the potential of applying to areas like aviation safety, where high-spatial-resolution wind measuring in complex environment is required.

References

[1] B. Witschas, S. Rahm, A. Dörnbrack, J. Wagner, and M. Rapp, "Airborne wind LiDAR measurements of vertical and horizontal winds for the investigation of orographically induced gravity waves," *J. Atmos. Ocean. Technol.*, vol. 34, no. 6, pp. 1371–1386, Jun. 2017.

[2] T. Mikkelsen, "LiDAR-based research and innovation at DTU wind energy—A review," *J. Phys., Conf.*, vol. 524, Jun. 2014, Art. no. 012007.

[3] Y. Yang et al., "Characteristics of heavy particulate matter pollution events over Hong Kong and their relationships with vertical wind profiles using high-time-resolution Doppler LiDAR measurements," *J. Geophys. Res., Atmos.*, vol. 124, no. 16, pp. 9609–9623, Aug. 2019.

[4] T. Wei, H. Xia, B. Yue, Y. Wu, and Q. Liu, "Remote sensing of raindrop size distribution using the coherent Doppler LiDAR," *Opt. Exp.*, vol. 29, no. 11, pp. 17246–17257, May 2021.

[5] I. N. Smalikho and V. A. Banakh, "Estimation of aircraft wake vortex parameters from data measured with a 1.5 μm coherent Doppler LiDAR," *Opt. Lett.*, vol. 40, no. 14, pp. 3408–3411, Jul. 2015.

[6] S. Wu, X. Zhai, and B. Liu, "Aircraft wake vortex and turbulence measurement under near-ground effect using coherent Doppler LiDAR," *Opt. Exp.*, vol. 27, no. 2, pp. 1142–1163, 2019.

[7] C. Liang, C. Wang, X. Xue, X. Dou, and T. Chen, "Meter-scale and sub-second-resolution coherent Doppler wind LiDAR and hyperfine wind observation," *Opt. Lett.*, vol. 47, no. 13, pp. 3179–3182, Jul. 2022.

[8] S. W. Henderson, P. Gatt, D. Rees, and R. M. Huffaker, "Wind LiDAR," in *Laser Remote Sensing*, T. Fujii and T. Fukuchi, Eds., Boca Raton, FL, USA: CRC, 2005, ch. 7, pp. 520–570.

[9] Y. Zhang, Y. Wu, and H. Xia, "Spatial resolution enhancement of coherent Doppler wind LiDAR using differential correlation pair technique," *Opt. Lett.*, vol. 46, no. 22, pp. 5550–5553, Nov. 2021.

[10] Y. Zhang, Y. Wu, and H. Xia, "High resolution coherent Doppler wind LiDAR incorporating phase-shift keying," *J. Lightw. Technol.*, vol. 40, no. 22, pp. 7471–7478, Nov. 15, 2022.

[11] F. Yang, Y. He, W. Chen, and Y. Zhan, "Laser altimeter based on random code phase modulation and heterodyne detection," *IEEE Photon. Technol. Lett.*, vol. 26, no. 23, pp. 2337–2340, Dec. 1, 2014.

[12] Y. Zhang, Y. Wu, and H. Xia, "Spatial resolution enhancement of coherent Doppler LiDAR by pseudo-random phase coding," *J. Lightw. Technol.*, vol. 40, no. 13, pp. 4467–4473, Jul. 1, 2022.

[13] D. Ba, Y. Li, J. Yan, X. Zhang, and Y. Dong, "Phase-coded Brillouin optical correlation domain analysis with 2-mm resolution based on phase-shift keying," *Opt. Exp.*, vol. 27, no. 25, pp. 36197–36205, Dec. 2019.

[14] N. Kotake et al., "Intelligent and compact coherent Doppler LiDAR with fiber-based configuration for robust wind sensing in various atmospheric and environmental conditions," *Opt. Exp.*, vol. 30, no. 11, pp. 20038–20062, May 2022.

[15] O. Kliebisch, H. Uittenbosch, J. Thurn, and P. Mahnke, "Coherent Doppler wind LiDAR with real-time wind processing and low signal-to-noise ratio reconstruction based on a convolutional neural network," *Opt. Exp.*, vol. 30, no. 4, pp. 5540–5552, Feb. 2022.

[16] P. Schroeder et al., "A compact, flexible, and robust micropulsed Doppler LiDAR," *J. Atmos. Ocean. Technol.*, vol. 37, no. 8, pp. 1387–1402, Aug. 2020.

[17] R. G. Frehlich and M. J. Yadlowsky, "Performance of mean-frequency estimators for Doppler radar and LiDAR," *J. Atmos. Ocean. Technol.*, vol. 11, no. 5, pp. 1217–1230, Oct. 1994.